THE ASTROPHYSICAL JOURNAL, 531:350–365, 2000 March 1

A RADIATION HYDRODYNAMIC MODEL FOR PROTOSTELLAR COLLAPSE. II. THE SECOND COLLAPSE AND THE BIRTH OF A PROTOSTAR

HIROHIKO MASUNAGA[1] AND SHU-ICHIRO INUTSUKA[2]
Division of Theoretical Astrophysics, National Astronomical Observatory, Mitaka, Tokyo 181-8588, Japan
Received 1999 April 19; accepted 1999 November 15

ABSTRACT

We carry out radiation hydrodynamic calculations to study physical processes in the formation of a 1 $M_\odot$ protostar. Following our previous work, calculations pursue the whole evolution from the beginning of the first collapse to the end of the main accretion phase. The adiabatic core formed after the initial collapse (i.e., the first core) experiences further gravitational collapse triggered by dissociation of molecular hydrogen, which leads to the formation of the second core, i.e., the birth of a protostar. The protostar grows in mass as accreting the infalling material from the circumstellar envelope, while the protostar keeps its radius at $\sim 4\ R_\odot$ during the main accretion phase. These typical features in the evolution are in good agreement with previous studies. We consider two different initial conditions for the density distribution: homogeneous and hydrostatic cloud cores with the same central density of 1.415×10^{-19} g cm^{-3}. The homogeneous core has the total mass of 1 $M_\odot$ while the hydrostatic core has 3.852 $M_\odot$. For the initially homogeneous model, the accretion luminosity rapidly rises to the maximum value of 25 $L_\odot$ just after the birth of a protostar, and declines gradually as the mass accretion rate decreases. In contrast, the luminosity increases monotonically with time for the initially hydrostatic model. This difference arises because the mass accretion rate varies depending on the inward acceleration at the initial stage, which affects the luminosity curve. A less massive hydrostatic core would possess the similar properties in the luminosity curve to the 3.852 $M_\odot$ case, because a hydrostatic cloud core with mass lower than 3.852 $M_\odot$ can be shown to provide a smaller mass accretion rate after the birth of a protostar and a more gradual rise in the luminosity curve. Our numerical code is designed to provide the evolution of the spectral energy distribution (SED) along with the dynamical evolution in our spherically symmetric calculations. We confirm that the SED evolves from a 10 K graybody spectrum to hotter spectra typical for class I and flat spectrum sources. The SED for the class 0 sources corresponds to the age of 2×10^4 yr, which is smaller by an order of magnitude than the typical age of class I objects. Considering possible nonspherically symmetric effects, we suggest that observed class 0 sources should consist of the "genuine" class 0 objects, which are as young as 10^4 yr, and more evolved protostars on edge-on view ("class 0–like class I" objects). The contamination of edge-on class I objects into class 0 sources are not negligible because they are more abundant than genuine class 0 objects. Since observations indicate that the class 0 sources are typically more luminous than class I sources, the initially hydrostatic model, where the luminosity increases monotonically with time, does not match the observations. The initially homogeneous model, in contrast, shows a tendency consistent with the observations. Compiling our results and other theoretical and observational evidence, we illustrate an evolutionary picture of protostar formation. In terms of the evolutionary time and the inclination to an observer, we find that protostellar objects are clearly categorized.

Subject headings: hydrodynamics — ISM: clouds — methods: numerical — radiative transfer — stars: formation

1. INTRODUCTION

Investigation of star formation processes has been a significant subject both for theoretical astrophysics and for observational astronomy. Nevertheless, many problems are to date unresolved, especially in the early phase in the evolution in which a protostar is under dynamical growth. The lack of our knowledge for protostar formation is a "missing link" in the evolutionary picture of star formation.

Objects at very early stages of the evolution are difficult to observe for the following two reasons: (1) a growing protostar is veiled by the infalling envelope, and (2) the timescale is relatively short for such young objects, so that the expected number of the objects is small. Recently, observations have made remarkable progress in the studies of protostar formation. André, Ward-Thompson, & Barsony (1993) proposed the "class 0" category for the objects of $L_{\rm bol}/L_{1.3} \lesssim 2 \times 10^4$, where $L_{1.3}$ is the 1.3 mm luminosity, and they considered class 0 sources as candidates for young protostars under dynamical growth. In addition to the above definition, Barsony (1994) listed some empirical characteristics for class 0 sources as follows: (1) no detection in the near- and mid-infrared, (2) a cold spectral energy distribution ($T \leq 30$ K), and (3) presence of a molecular outflow. While the class 0 category has become familiar, its evolutionary position is not confirmed by detailed theoretical calculations. Past theoretical studies on protostar formation (Winkler & Newman 1980a, 1980b, hereafter WN collectively; Stahler, Shu, & Taam 1980, hereafter SST, and references therein) were not designed to explain the recent

[1] Present address: Earth Observation Research Center, National Space Development Agency of Japan, 1-9-9 Roppongi, Minato-ku, Tokyo 106-0032 Japan; masunaga@ccsr.u-tokyo.ac.jp.
[2] inutsuka@th.nao.ac.jp.

observations by means of observable quantities such as spectral energy distributions and molecular line spectra. Now a theoretical model for protostar formation and its spectral synthesis are required to account for latest observations. This motivates us to a series of this study, which started with our previous paper (Masunaga, Miyama, & Inutsuka 1998, hereafter Paper I). We have also performed model calculations for line spectral synthesis, which are presented in Masunaga & Inutsuka (2000).

We have developed a radiation hydrodynamic (RHD) numerical code in spherical symmetry, where the angle- and frequency-dependent radiative transfer equation is solved along with a full set of the radiation hydrodynamic equations. Therefore our calculations invoke neither the Eddington (and diffusion) approximation nor the gray approximation. In addition, the monochromatic radiative transfer equation provides spectral energy distributions (SEDs), and the evolution of a SED is obtained as well as the dynamical evolution from our numerical results. This enables us to compare computational results directly with observations.

In Paper I, we investigated the evolution of protostellar collapse before the formation of a protostar. Main subjects of Paper I are the gravitational collapse of molecular cloud cores (the so-called first collapse), violation of the isothermal evolution (discussed further in Masunaga & Inutsuka 1999a), and the formation of a central adiabatic core (the first core). Previous versions of our numerical code did not include dissociation of molecular hydrogen, and thus the evolution succeeding to the first collapse was outside the scope of Paper I because the first core experiences further gravitational collapse (i.e., the second collapse) triggered by dissociation of H_2, which leads to the birth of a protostar. The present version of the code takes into account all the necessary physical processes (described in § 2.1) in order to pursue the entire evolution from gravitational collapse of a molecular cloud core to the end of mass accretion from the infalling gas envelope onto a protostar. A main purpose of this paper is to construct a theoretical model for protostar formation incorporating updated data for EOS and opacities that were not available in days of WN and SST.

Another important aim of the present work is to clarify evolutionary positions of observed protostellar objects (starless cores, class 0 sources, etc.) in terms of SEDs and bolometric temperatures (Myers & Ladd 1993). Some recent theoretical studies yielded SEDs of protostellar objects by multidimensional RHD calculations, where the calculation stopped before a protostar is born (the "class I" phase; Boss & Yorke 1995) or a protostar is put as a central luminosity source (Yorke, Bodenheimer, & Laughlin 1993, 1995). Their calculations used the Eddington approximation (Boss & Yorke 1995) or the flux-limited diffusion approximation (Yorke et al. 1993, 1995) for simplicity, where the hydrodynamic quantities and radiation fields are not treated in a self-consistent way. In this work we have established comprehensive theoretical models for the whole evolution of a protostar, solving self-consistently the physical structures of the protostellar interior and the circumstellar envelope.

In § 2.1 we explain the revisions that have been made since our previous work in the numerical scheme and in the input physical processes. Computational results are shown in § 3, where the evolutionary process in protostar formation is described in terms of the hydrodynamical quantities, SEDs, and luminosity curves. Section 4 is devoted to discussions on the relations between our results and statistical trends in observations. We there illustrate an evolutionary picture of protostar formation by taking into account expected nonspherically symmetric effects. Conclusions are summarized in § 5. The basic equations that we solve in numerical calculations are shown in Appendix.

2. CALCULATIONS

2.1. *Numerical Scheme and Input Physics*

As a computational scheme for handling radiation hydrodynamics, we adopt the variable Eddington factor (VEF) method, where we solve the system of the hydrodynamic equations and the radiation moment equations which are coupled with the angle-dependent radiative transfer equation via the variable Eddington factor. The VEF method enables us to solve the RHD equations with a desirable accuracy and with a reasonable computational cost. In contrast to WN, who also adopted this method, we have designed our scheme to yield SEDs as computational byproducts by considering the monochromatic radiative transfer. Detail on the computational procedure of the VEF method is described in Paper I.

Although the outline of our numerical scheme remains unchanged throughout the revisions, some significant improvements have been made in the numerical code since Paper I, as summarized in the following:

1. Input physical processes are more elaborate in the present version. Dissociation of molecular hydrogen, ionization of atomic hydrogen and helium, and nonideal equation of state (EOS) have been incorporated. We use the tabulated data provided by Saumon, Chablier, & Van Horn (1995) for the nonideal EOS. The specific heat of molecular hydrogen, which was given as a constant in Paper I, is now calculated as a function of temperature by solving the partition functions for the rotational and vibrational energy levels of H_2 in addition to the translational component.

2. The gas and dust opacities have been also improved. The gas opacity is taken from Iglesias & Rogers (1996) in the high-temperature regime [$\log T(\mathrm{K}) > 3.75$] and from Alexander & Ferguson (1994) for lower temperatures. The dust opacity was provided by H. W. Yorke (1998, private communication), where the three components, i.e., amorphous carbon, silicate, and dirty ice-coated silicate, are considered on the basis of the opacity model by Preibisch et al. (1993). The scattering by dust grains are taken into account as well as the absorption.

3. The dust temperatures are solved independently of the gas temperature, while they are assumed to be the same in WN, SST, and Paper I. The dust and gas temperatures are decoupled with each other when the density is so low that the exchange of the thermal energy by collisions between gas and dust grains are less effective. Such a situation is found to occur where the infalling envelope becomes tenuous in the late stages of the evolution.

See Masunaga (1999) for more detailed descriptions on the input physical processes and on the numerical scheme.

2.2. *Initial Density Structure*

An appropriate initial condition for gravitational collapse of a cloud core is related with mechanism for the initiation of star formation, which involves a controversial

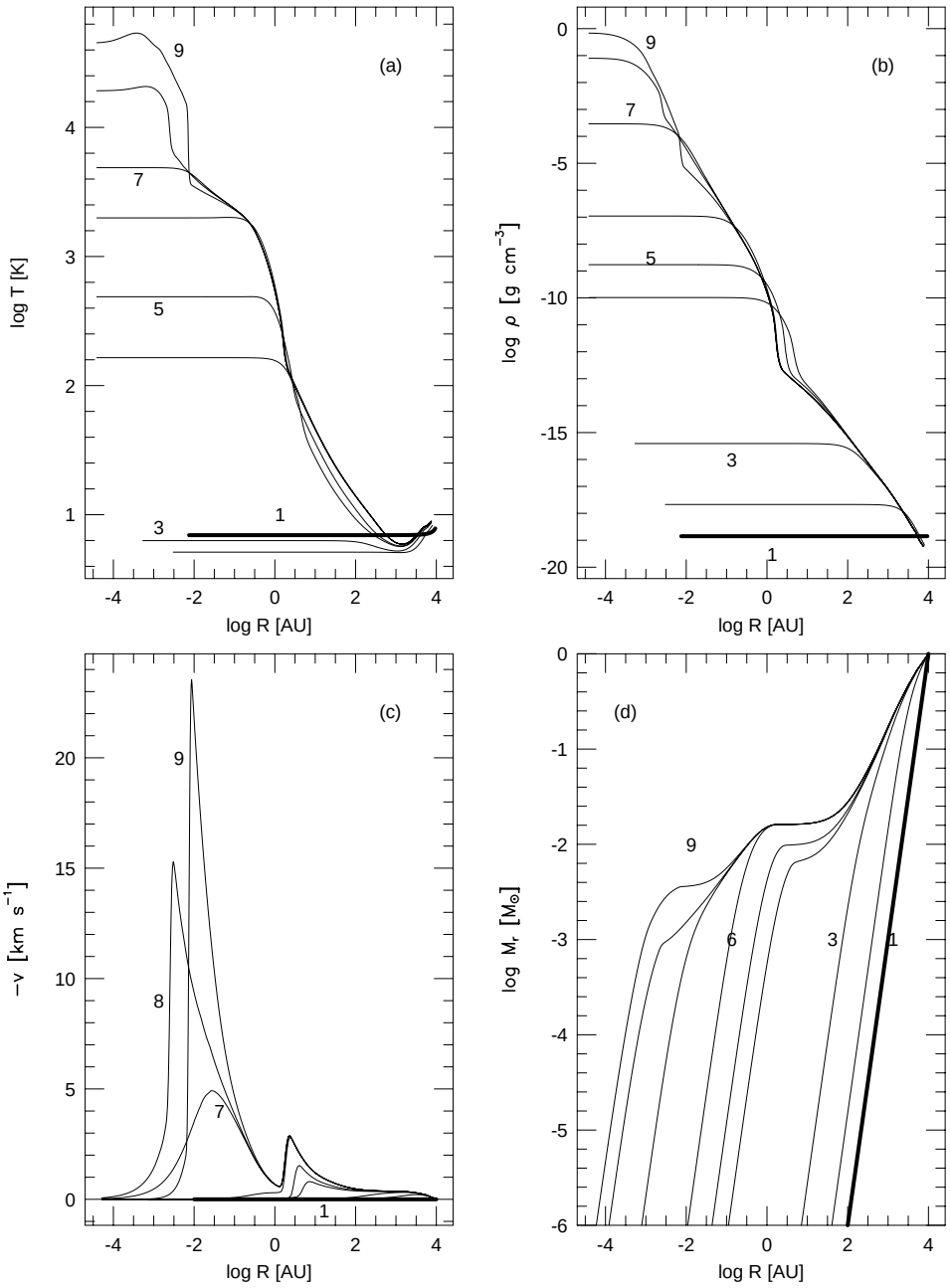

FIG. 1.—Numerical results for the initially homogeneous model before the main accretion phase begins are shown. The succeeding evolution is depicted in Fig. 4. Distributions of temperature (*a*), density (*b*), infall velocity (*c*), and mass (*d*) are presented. Thick line denotes the initial condition. Elapsed times are tabulated in Table 1.

problem. Star formation may be triggered by external factors such as shock compression of gas due to supernovae or stellar winds in the neighborhood of star formation regions. Otherwise, a star formation may occur spontaneously because of the plasma drift (or the ambipolar diffusion) of magnetic fields (e.g., Nakano 1979; Shu 1995; and references therein) or the dissipation of turbulence which reduces the effective sound velocity in cloud cores (Nakano 1998). The "spontaneous star formation" process would produce nearly hydrostatic cloud cores as the initial condition for the dynamical collapse, while the "triggered star formation" would not necessarily. Although some recent observations resolved spatial structures of molecular cloud cores, the initial condition is still difficult to determine from observational evidence.

Larson (1969, hereafter L69) and WN supposed a homogeneous distribution as the initial density structure in their calculations for protostar formation. A homogeneous cloud core is not in hydrostatic equilibrium and hence the gravitational collapse is initiated with a considerable inward acceleration. The dynamical evolution is known to be insensitive to the initial density configuration (Bodenheimer & Sweigart 1968; Paper I), unless the gravitational energy is significantly larger than the thermal energy at the initial stage. Nevertheless, different initial conditions for the density distribution may cause a small difference in the mass accretion rate, which possibly hastens or retards the growth of a protostar.

In this paper, two limiting cases are considered for the initial density distribution: the homogeneous distribution

and the hydrostatic distribution. The homogeneous cloud core has a total mass of 1 $M_\odot$ and is bounded by the fixed boundary at $R = 10^4$ AU, which yields the density of 1.415×10^{-19}g cm^{-3}. This condition is equivalent to those by L69 and WN. The hydrostatic distribution is obtained by solving the equation of hydrostatic equilibrium for an isothermal sphere:

$$\frac{1}{r^2}\frac{d}{dr}\left(\frac{r^2}{\rho}\frac{d\rho}{dr}\right) = -\frac{4\pi G\rho}{c_s^2}, \quad (1)$$

where c_s is the isothermal sound speed. We numerically integrate equation (1) outwardly from the center with the same central density as in the homogeneous model (i.e., $\rho_c \equiv 1.415 \times 10^{-19}$). For the initially hydrostatic models the outer boundary is fixed at $R = 4 \times 10^4$ AU and the total mass is then found to be 3.852 $M_\odot$. We adopt a larger value of the total mass than in the homogeneous model because the mass should exceed a critical value so that an isothermal hydrostatic core is gravitationally unstable (Ebert 1955; Bonner 1956).

2.3. *Initial Temperature Structure*

For the thermal energy balance at the initial stage, we consider a more realistic condition than in Paper I and than in any other works concerned with protostar formation. Previous studies assumed isotropic blackbody radiation of 10 K surrounding the cloud core (L69; WN) or heat sources embedded homogeneously with no incident radiation (Paper I). In contrast, the initial temperature profile here is taken as the thermal equilibrium state between the thermal cooling of dust grains and the heating by the external radiation and cosmic rays (e.g., Hayashi & Nakano 1965). The external radiation field considered here is the sum of the background radiation of 2.7K and ambient stellar radiation. Stellar photons are given as diluted blackbody radiation of 6000 K with the intensity integrated over frequency of 2×10^{-4} ergs s^{-1} cm^{-2} for the initially homogeneous model and 1×10^{-4} ergs s^{-1} cm^{-2} for the initially hydrostatic model. We obtain the equilibrium state by solving numerically the radiation moment equations and the energy equation under the fixed density distribution. The stellar radiation sustains the cloud core to be nearly 10 K (Hayashi & Nakano 1965) with the cosmic ray heating rate of $\epsilon_{CR} = 6.4 \times 10^{-28} n(H_2)$ ergs s^{-1}cm^{-3} (Goldsmith & Langer 1978). The initial cloud core has an optical depth close to unity to optical photons. Incident optical photons, therefore, are attenuated as passing through the cloud core and the temperature in deep interior is slightly lower than the temperature near the cloud edge (see Fig. 1).

In order to consider the thermal balance between the thermal cooling and external radiation, a frequency-dependent treatment for radiation transport is imperative. The dust opacity for optical wavelengths is larger by 4 orders of magnitude than the value for the submillimeter and then gray approximations are totally invalid.

3. RESULTS

3.1. *Overview*

We present computational results of protostellar collapse of an initially homogeneous cloud core. The result of the initially hydrostatic model is found to be qualitatively the same as the initially homogeneous one except for the behavior of the luminosity curve. Hence we describe the evolutionary properties only for the initially homogeneous model in this section, and the luminosity curve will be discussed for each case in § 3.2.

3.1.1. *The Early Isothermal Phase*

Figure 1 shows the evolution before a protostar is born. Evolution at the early stage, i.e., the first collapse stage, proceeds along the line described in Paper I, where the density distribution is reminiscent of the isothermal self-similar solutions such as the so-called Larson-Penston solution (L69; Penston 1969, hereafter the LP solution). The results are consistent with Foster & Chevalier (1993), where a numerical calculation was performed for the isothermal collapse of a marginally unstable sphere. A major difference from Paper I arises in the thermal evolution because of the more realistic assumption for the external radiation field (§ 2.3). In contrast to the previous models, where the temperature never descends below the initial value, temperature in the central region once decreases to $\sim$5 K and then rises again. The reason for the decrease of T is that increasing column density of the collapsing cloud core prevents optical photons from penetrating into the interior. The cloud core then cools down to 5 K, at which the cosmic ray heating support the temperature against the thermal cooling. However, the compressional heating rate (Γ_g) immediately overtakes the thermal cooling rate ($4\pi\kappa_P B$) at $\rho_c \approx 10^{-17}$ g cm^{-3}, where all the lines except $\kappa_E cE$ are merged, and the central temperature begins to increase (Fig. 2). This behavior is supported by a result in our previous work (§ 3.1 in Paper I), where the isothermal evolution of a cloud core of $T = 5$ K was found to cease very early at $\rho_c \sim \rho_{\Lambda=\Gamma} = 8.8 \times 10^{-18}$ g cm^{-3}. Cooling of gas due to collisions with dust grains (Λ_{gd} in Fig. 2*a*) is closely coupled with the radiative cooling rate and with the compressional heating rate for $\rho_c \gtrsim 10^{-17}$ g cm^{-3}.

3.1.2. *The First Core*

Although the central temperature begins to rise far before the optical depth arrives at unity, the evolution becomes completely adiabatic when $\tau \approx 1$ at $\rho_c \approx 10^{-12}$ g cm^{-3}, at which the radiative heating rate ($\kappa_E cE$) overtakes the radiative cooling rate. For adiabatic evolutions the effective adiabatic exponent, $\gamma_{\rm eff} \equiv d\ln T/d\ln\rho + 1$, equals the ratio of specific heats ($\gamma_{\rm eff} = 7/5$ for $T \gtrsim 100$ K) as one can seen in Figure 2*b*. The gravitational collapse is decelerated by the increasing gas pressure, which leads to the formation of the first core. The physical properties of the first collapse and first core were discussed in detail in Paper I. Typical scales of radius and mass of the first core agree with the values obtained there. We do not repeat further discussions on the first collapse here.

3.1.3. *The Second Collapse*

The second collapse takes place (curves 6–8 in Fig. 1) when the central density and the central temperature reach $\rho_c \sim 10^{-7}$ g cm^{-3} and $T_c \sim 2000$ K, where dissociation of molecular hydrogen reduces the effective adiabatic exponent to $\sim$1.1. Dissociation of H_2 ceases when the dissociation degree approaches unity in the center at $\rho_c \sim 10^{-2}$ and $T_c \sim 10^4$ K. This is the instance when the second core is formed, i.e., when a protostar is born. The dynamical timescale of the second collapse is of the same order as the free-fall time corresponding to $\rho = 10^{-7}$ g cm^{-3}, which is 0.1 yr. The second collapse therefore begins and ends almost instantaneously compared to the first collapse, which lasts

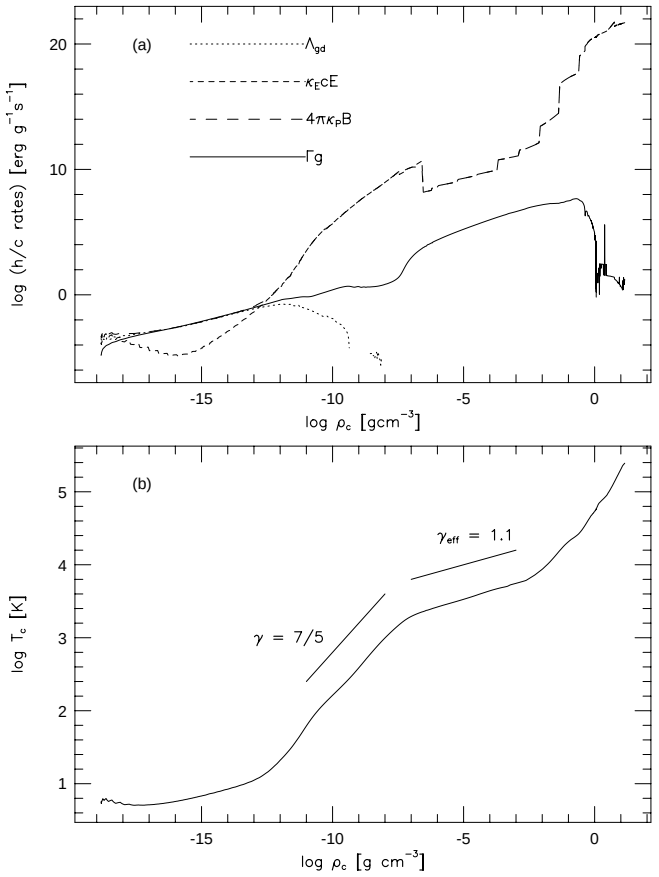

FIG. 2.—Thermal evolution at the center of the cloud core is depicted for the initially homogeneous model. The upper panel shows the energy exchange rate between gas and dust (Λ_{gd}), the radiative heating rate ($\kappa_E cE$), the radiative cooling rate ($4\pi\kappa_P B$), and the compressional heating rate of Γ_g) as functions of the central density. For $\rho_c \gtrsim 10^{-12}$ g cm^{-3} the radiative heating and cooling rates are merged. The lower panel shows the central temperature as a function of the central density.

for a free-fall time of the initial cloud core, i.e.,

$$t_{\rm ff} = \frac{\pi}{2}\sqrt{\frac{R^3}{2GM}} = 1.77 \times 10^5 \text{ yr} . \quad (2)$$

The adiabat recovers its steepness after the second collapse is halted, but $\gamma_{\rm eff}$ does not reach 5/3 as expected for monoatomic gas because the partial degeneracy of electrons begins to dominates the pressure in the center.

All the components of dust grains evaporate at $\rho_c \sim 3 \times 10^{-7}$ g cm^{-3} and the radiative heating and cooling rates drop suddenly. The increasing density and temperature, however, again raise the radiative heating and cooling rates. The compressional heating rate of gas increases with ρ_c until the collapse is almost halted at $\rho_c \sim 1$ g cm^{-3}, where the compressional heating rate drops by more than 6 orders of magnitude and the quasi-static contraction of the protostar follows instead of the dynamical collapse.

3.1.4. *The Birth of a Protostar*

L69 and WN reported rebound of the second core just after its formation. In our results, indeed, a shock wave propagates outward as if the second core rebounded (see Fig. 1*c*). The rebound, however, does not actually occur because the velocity always remains negative everywhere.

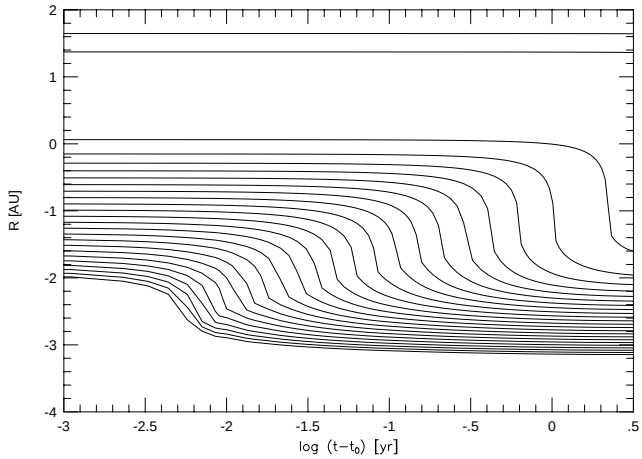

FIG. 3.—Trajectories of mass elements of the cloud core are delineated just after the second collapse. The innermost and uppermost mass shells correspond to $M_r = 10^{-3}\ M_\odot$ and $M_r = 2 \times 10^{-2}\ M_\odot$, respectively. Difference in mass between the neighboring shells is constant in logarithmic scale, where $\Delta \log M_r = 5.42 \times 10^{-2}$. See legend of Table 1 for the definition of t_0.

The feature that the infalling gas is decelerated (but not reversed) by an outgoing shock wave is observed more clearly in Figure 3, which illustrates the trajectories of mass elements during the second collapse. Here the offset of time, $t_0 \equiv 1.7526 \times 10^5$ yr, is taken as the instance when the second collapse begins (Table 1). As expected, t_0 is very close to $t_{\rm ff}$ defined by equation (2). A shock wave propagates outwardly as settling the infalling material onto the second core.

The very short second collapse phase is followed by the main accretion phase (curves 9–13 in Fig. 4), where the central protostar grows in mass by the steady accretion from the infalling envelope. The duration time of the main accretion phase is characterized by the accretion time, $t_{\rm acc}$, which is defined by the time required for a mass element in

TABLE 1

ELAPSED TIMES FOR THE INITIALLY HOMOGENEOUS MODEL

Label	$t - t_0$ (yr) [a]
1	-1.7522×10^5
2	-2.9237×10^4
3	-4.1894×10^3
4	-6.5192×10^2
5	-4.3844×10^2
6	-1.2656×10^0
7	-3.1250×10^{-2}
8	-1.5625×10^{-2}
9	1.5625×10^{-2}
10.....	1.8984×10^1
11.....	4.9265×10^3
12.....	2.2958×10^4
13.....	1.3788×10^5

a The offset of time, $t_0 \equiv 1.7526 \times 10^5$ yr, represents the instance when the second collapse begins.

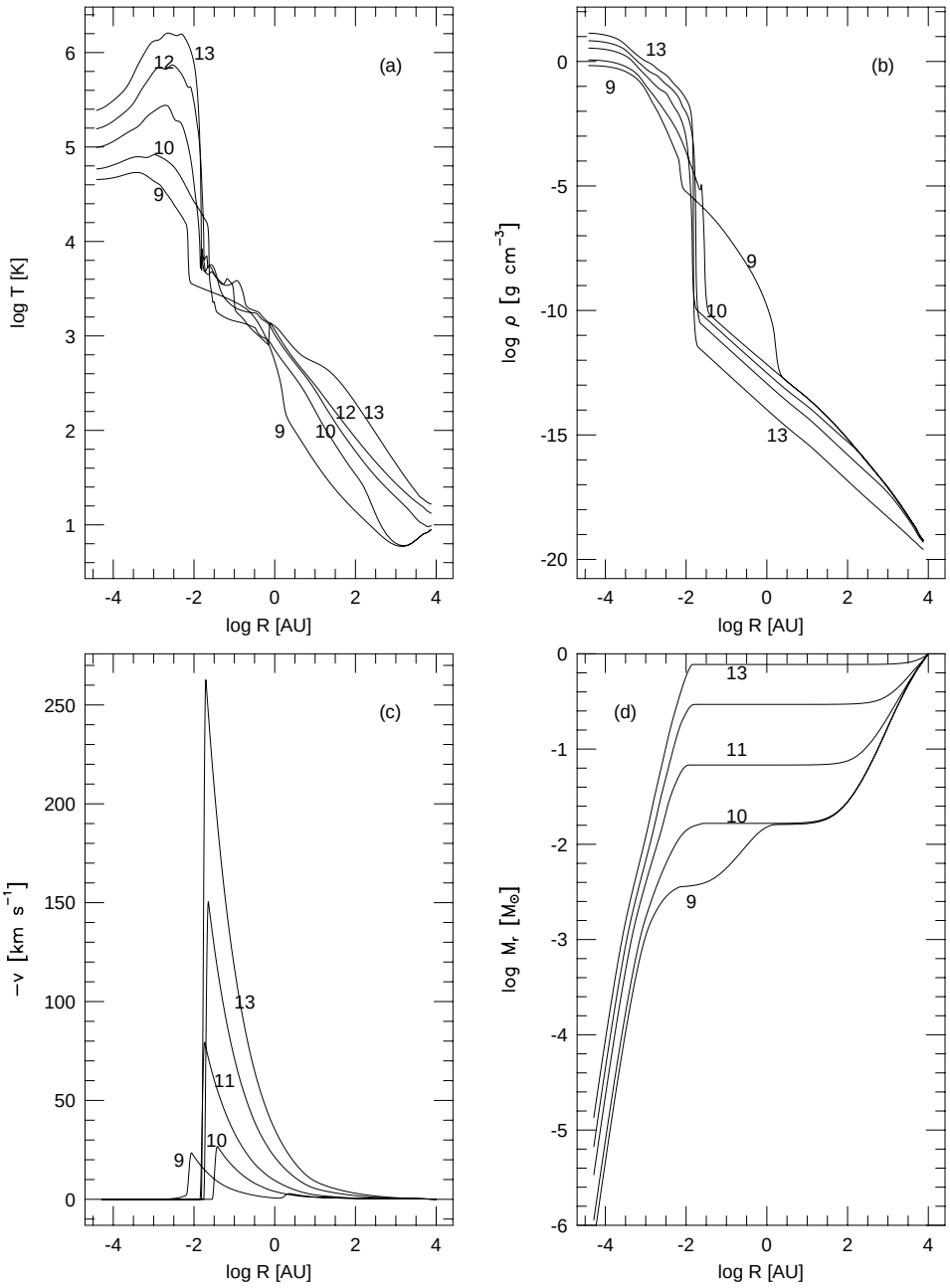

FIG. 4.—Numerical results for the initially homogeneous model in the main accretion phase are shown. The preceding evolution is depicted in Fig. 1. Elapsed times are tabulated in Table 1.

the infalling envelope to be settled on the central star:

$$t_{\rm acc} \simeq \frac{R}{v_{\rm ff}}\,, \tag{3}$$

where R is the radius of the infalling envelope, and $v_{\rm ff} \equiv \sqrt{2GM/R}$ is the free-fall velocity. Rearranging equation (3), we obtain

$$t_{\rm acc} \simeq \sqrt{\frac{R^3}{2GM}}\,, \tag{4}$$

which gives essentially the same value as the free-fall time (eq. [2]) except for numerical factors of order of unity.

Figure 4 shows the evolution succeeding to Figure 1. The second core, which is a "seed" of a protostar, grows monotonically in mass as accreting the infalling material (Fig. 4*d*). The radius of the protostar, which is indicated by the "wall" in the density distribution (Fig. 4*b*), is settled at 2×10^{-2} AU or 4 $R_\odot$ during the main accretion phase. This value of the protostellar radius is in agreement with WN and SST.

3.1.5. *The Temperature Profile in the Protostar*

The internal structure of the protostar shows an off-centered peak in the temperature distribution, as also found by WN and SST. The off-centered maximum of temperature arises because of partially degenerate electrons in the central region. Since the pressure of degenerate gas depends only weakly upon temperature, the gravitational contraction of the protostar does not raise temperature effectively where degenerate gas dominates the pressure. In the off-centered region where the density is not high enough and

the thermal energy dominates the Fermi energy, the gas pressure is more sensitive to temperature and the off-centered temperature becomes higher than in the center.

3.1.6. *The Infalling Envelope*

The density structure in the infalling envelope is approximately $\rho \propto r^{-1.5}$ in the inner region and $\rho \propto r^{-2}$ in the outer, and the boundary between these regions shifts outwardly with time. This feature resembles the singular isothermal self-similar solutions, e.g., the solutions obtained by Shu (1977) along with expansion-wave solution and those by Hunter (1977) which include the continuous counterpart of the LP solution.

Plateau in the mass distribution (Fig. 4*d*) indicates the current mass of the central protostar. The protostellar mass monotonically reaches 0.73 $M_\odot$ at the end of the calculation.

3.1.7. *The Radiation Field*

The upper panel in Figure 5 depicts spatial distributions of the Eddington factor in the main accretion phase. The Eddington factor is kept at $\frac{1}{3}$ in the protostellar interior ($R \lesssim 10^{-2}$AU), where the optical depth is quite large ($\tau \sim 10^{15}$). At the accretion shock front on the protostellar surface the Eddington factor sharply drops below $\frac{1}{3}$, which occurs because the optically thin radiative relaxation layer, where the shocked gas cools down by radiating away its thermal energy, is filled with radiation hotter than in the preshock gas and the postrelaxation layer (Fig. 6; see legend

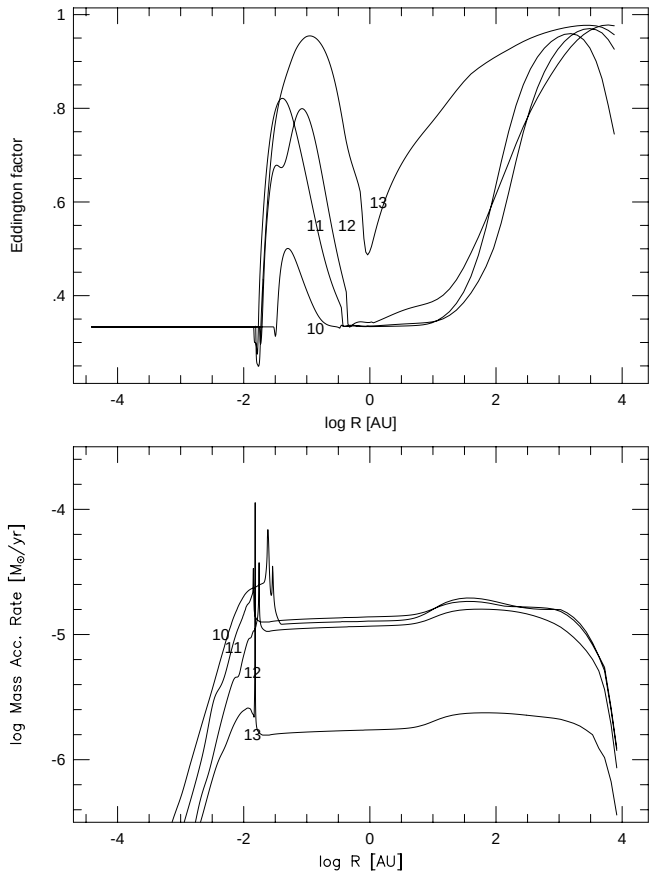

FIG. 5.—Upper panel depicts the Eddington factor as a function of radius in the main accretion phase. Elapsed times are tabulated in Table 1. The lower panel shows the mass accretion rate, i.e., $\dot{M}(r) \equiv 4\pi r^2 \rho(r)[-v(r)]$.

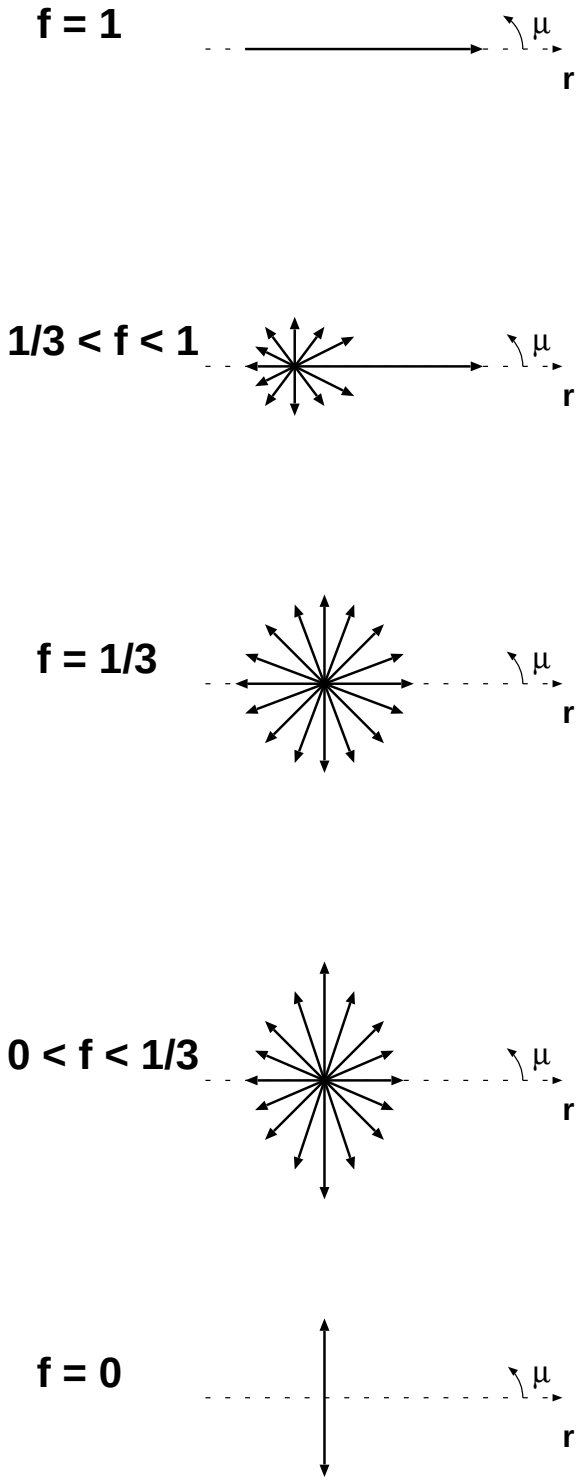

FIG. 6.—Schematic picture for the Eddington factor, $f \equiv \int_{-1}^{1} I\mu^2 d\mu / \int_{-1}^{1} I d\mu$, is illustrated. Arrows represent the angular distribution of the specific intensity, I. A special case where the Eddington factor drops below $\frac{1}{3}$ as well is shown. For the isotropic radiation field (I = constant), $f = \frac{1}{3}$ (*middle*). As the radiation field becomes outwardly peaking (e.g., the central luminous source with a diffuse and extended radiation field) f increases toward unity, which is the extreme case where only radial component exists [$I \propto \delta(\mu - 1)$] (*top*). In contrast, f descends below $\frac{1}{3}$ where the radial component of the radiation field is dominated by the orthogonal component, and f falls onto zero in another extreme case where $I \propto \delta(\mu)$ (*bottom*). This case occurs near the strong radiation shock front, where the narrow radiation relaxation layer filled with hot radiation is sandwiched between the adjacent cool preshock and postrelaxation layers.

for more details; see also Balluch 1988). The Eddington factor rapidly rises toward 1 since the Planck-mean optical depth is smaller than unity between the protostellar surface and the dust sublimation front, at which the dust grains vapor away, but it decreases again onto $\frac{1}{3}$ near the dust sublimation front because the opaque dusty envelope reprocesses the outwardly peaking radiation from the center into a nearly isotropic field of the thermal radiation emitted by dust grains. The Eddington factor increases with radius once again as the dusty envelope becomes diffuse and the outwardly peaking radiation dominates the isotropic field. At the final stage (curve 13) the Eddington factor departs from $\frac{1}{3}$ even near the dust sublimation front. This is because the entire dusty envelope turns to be optically thin due to the depletion of the infalling material.

The lower panel in Figure 5 shows the distribution of the mass accretion rate, $\dot{M}$. On the protostellar surface $\dot{M}(r)$ has a sharp spike where the infalled material through the diffuse envelope settles onto the dense protostar. The mass accretion rate in the infalling envelope ($R \gg 10^{-2}$ AU) is $\sim 10^{-5}$ $M_\odot$ yr^{-1} independently of radius except near the outer edge in the early main accretion phase (curves 10–12). This value of $\dot{M}$ is consistent with SST, who adopted $\dot{M} \equiv 10^{-5}$ $M_\odot$ yr^{-1} $\sim c_{s0}^3/G$ as a free parameter, where c_{s0} is the effective sound velocity in the initial cloud core, However, $\dot{M}$ decreases to $\sim 10^{-6}$ $M_\odot$ yr^{-1} (curve 13) at later stages in the main accretion phase. Our calculation supposes no incident mass flux through the outer boundary and therefore the mass accretion rate should decline after a significant fraction of the total mass is accreted by the protostar.

The mass accretion rate shows a somewhat different behavior in the initially hydrostatic model, as seen in § 3.2 below.

3.2. *Luminosity Curves*

While the luminosity remains $\lesssim 0.01$ $L_\odot$ during the first collapse as shown in Paper I, it rapidly rises when the second core, or a protostar, is born. The luminosity reaches the maximum value of ≈ 25 $L_\odot$ and then decreases gradually in the initially homogeneous model (Fig. 7). The luminosity of a protostar surrounded by an infalling envelope is dominated by the accretion luminosity:

$$L_{\rm acc}(t) = \frac{GM_*(t)\dot{M}_*(t)}{R_*(t)} = \frac{G\dot{M}_*(t)}{R_*(t)} \int_{t_0}^{t} \dot{M}_*(t')\, dt' , \qquad (5)$$

where M_* is the protostellar mass, R_* is the protostellar radius, and $\dot{M}_*$ is the mass accretion rate onto the protostar. As the protostellar radius is settled at 4 $R_\odot$ during the main accretion phase (§3.1), the shape of the luminosity curve reflects the time evolution of M_* and $\dot{M}_*$, which closely relate with each other. The initial rise in the luminosity curve is produced by the rapid growth of the protostellar mass. The luminosity declines after then because of the decreasing mass accretion rate, which is seen as a declining solid curve in the lower panel in Figure 7. The time-averaged mass accretion rate reads 5.7×10^{-6} $M_\odot$ yr^{-1} ($0 < t - t_0 < 1.4 \times 10^5$ yr) from the gradient of the M_*-t curve, while $\dot{M}_*$ just after the birth of a protostar is 1.3×10^{-5} $M_\odot$ yr^{-1}.

A homogeneous cloud core begins the gravitational collapse with inward acceleration because it has no pressure gradient and thus the force balance is not satisfied initially against the self-gravity. On the other hand, collapse of a

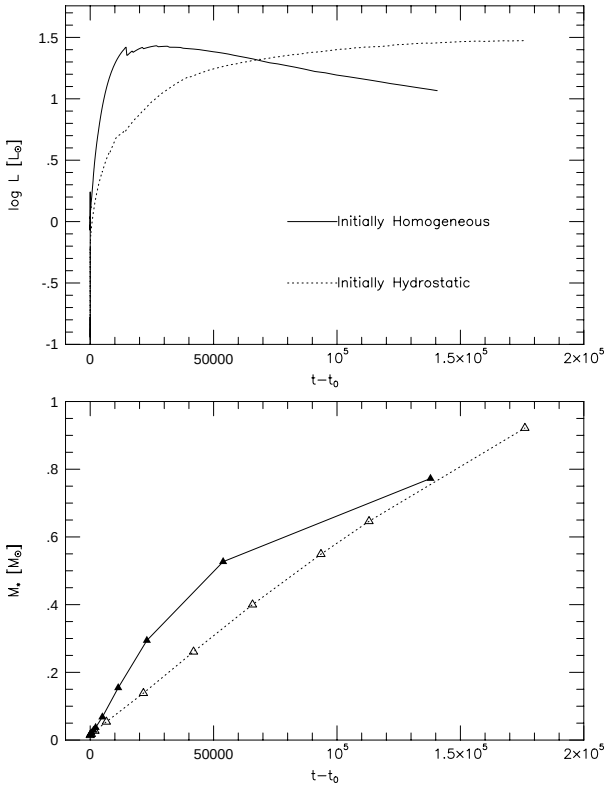

FIG. 7.—Luminosity curve (*upper panel*) and the protostellar mass (*lower panel*) are shown as functions of time after a protostar is formed. t_0 is defined in Table 1. Solid and dotted lines denote the initially homogeneous model and the initially hydrostatic model, respectively.

hydrostatic cloud core is initiated without significant acceleration, which yields a lower mass accretion rate than in the initially homogeneous case. Although the dynamical evolution "forgets" the initial density profile in the sound-crossing time (Paper I), small surviving influence on the mass accretion rate causes a qualitative difference in the behavior of the luminosity curve as seen in Figure 7.

In contrast to the initially homogeneous model, the initially hydrostatic model produces neither a rapid rise for $t \gtrsim t_0$ nor a decrease after the maximum in the luminosity curve, and instead shows a gradual and monotonic increase of the luminosity. The M_*-t diagram presents a linear growth of the protostellar mass for this model, which indicates that the mass accretion rate remains nearly constant. Lack of the rapid growth of M_* disables the abrupt rise in the luminosity curve at an early stage, and prevents immediate exhaustion of the infalling material, which is responsible for the decrease of the luminosity. The mass accretion rate is5.3×10^{-6} $M_\odot$ yr^{-1}, which is very close to the time-averaged value in the initially homogeneous model. The self-similar collapse solutions yield the mass accretion rate of a factor times c_s^3/G independently of the initial density configuration and of the total mass of a cloud core, which explains the reason why the time-averaged mass accretion rates in the two models accord with each other. Nevertheless, the mass accretion rate as a function of time exhibits different behaviors depending on the initial condition and the luminosity curve sensitively reflects the difference in $\dot{M}$ between the two models.

The difference in the total mass also influences the behavior of the luminosity curve. A less massive hydrostatic core

should be more centrally condensed so as to be gravitationally unstable, and hence the free-fall time ($\propto 1/\sqrt{G\rho}$) is shorter. In contrast, the condition when a protostar is born depends on neither the initial configuration nor the total mass of a cloud core because the condition of the violation of isothermality depends only on the initial temperature and opacity (Masunaga & Inutsuka 1999a). This means that a less massive cloud core is not allowed to spend sufficient time before the birth of a protostar to raise the mass accretion rate as large as that for a more massive cloud core. In other words, the first collapse phase of a less massive core is ended at an earlier stage when the convergence to the LP solution is less complete. As a consequence, any hydrostatic cloud cores would yield only a gradual rise in the luminosity curve after the birth of a protostar unless the total mass is substantially larger than 3.852 $M_\odot$. A less massive hydrostatic core, say a 1 $M_\odot$ core, should therefore possess the similar properties in the luminosity curve to the 3.852 $M_\odot$ case, and the difference in the total mass is not responsible for the different behavior in the luminosity curves between our initially homogeneous and hydrostatic models.

SST found that L increases monotonically with time. Evidently this increase of L shown by SST originates their "steady state approximation" in which $\dot{M}_*$ is fixed at 10^{-5} $M_\odot$ yr^{-1} throughout the calculation, where $L_{\rm acc}$ inevitably rises as the central protostar grows in mass. The steady state approximation by SST is valid for our initially hydrostatic model but is invalid for the initially homogeneous model. WN adopted a homogeneous cloud core as the initial condition, and thus they found the same tendency as in our initially homogeneous model on the contrary to SST.

Even for the initially homogeneous model where the luminosity declines with time, the final value of the luminosity (~ 10 $L_\odot$) is still too high for the typical value for class I sources (~ 1 $L_\odot$, Kenyon et al. 1990). This "luminosity problem" for class I protostars, which was pointed out by Kenyon et al. (1990), indeed arose in our spherically symmetric calculation. The luminosity problem, however, can be resolved by considering a possible difference in the mass accretion rates between the circumstellar disk and the infalling envelope (Kenyon, Calvet, & Hartmann 1993), which is not taken into account in our spherically symmetric calculations.

Exhaustion of the infalling material in our calculations is simply due to the condition that no mass flux should enter through the boundary. Physical mechanism which halts the mass accretion onto a protostar would include complicated processes for actual YSOs. Nakano, Hasegawa, & Norman (1995) showed that the mass outflows from YSOs finally halt further mass accretion by blowing off the residual envelope matter until the envelope becomes no longer gravitationally bound. This effect would suppress $\dot{M}_*$ at late stages of the evolution, which may also contribute to resolve the luminosity problem.

Which of the decreasing or increasing luminosity accounts for observations? To discuss observational counterparts of our results, we present results of SEDs in the next section.

3.3. *Spectral Energy Distributions*

The computational result for the emergent SED in the initially homogeneous model is shown in Figure 8. The SEDs are calculated from the monochromatic outgoing radiation through the cloud edge, convolved by the Gaussian beam pattern with a given FWHM. In Figure 8 an imaginary telescope is assumed to observe the object at a distance of 150 pc with the resolution of 10″ (FWHM). The interstellar extinction is not considered.

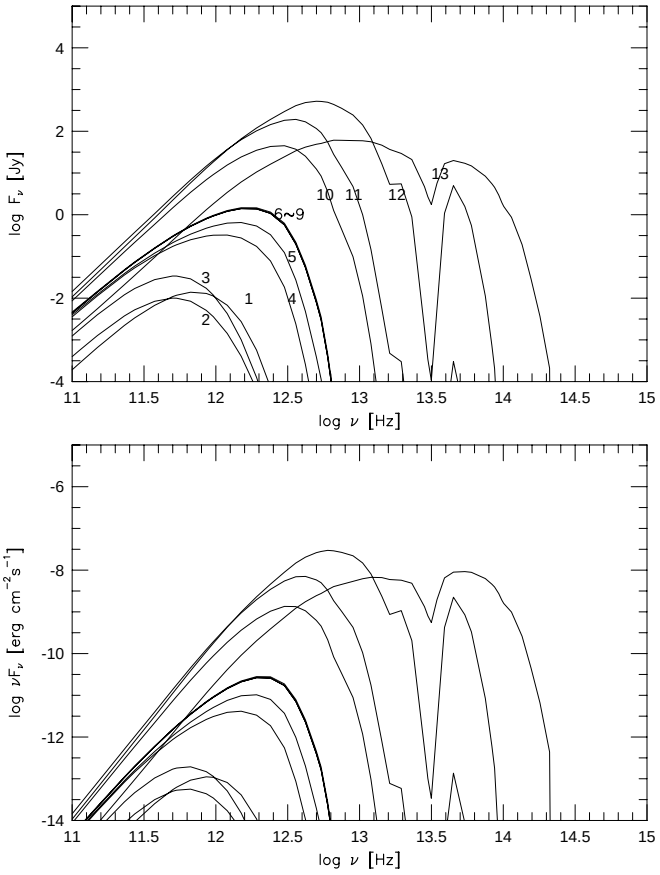

FIG. 8.—Evolution of the spectral energy distribution for the initially homogeneous model is shown. Elapsed time of each curve is listed in Table 1. The upper panel delineates the emergent flux, F_ν, in the unit of Jy, while the lower panel depicts νF_ν in the cgs unit. An observer is assumed to be at a distance of 150 pc with a telescope of the resolution of 10″.

At the initial stage the SED reflects optically thin thermal emissions by dust grains of nearly 10 K (the curve denoted by "1"). The SED once becomes colder (curves 2 and 3), due to a slight decrease of temperature mentioned in § 3.1, and then gradually becomes hotter. However, the first collapse stage (curves 1–6) shows no apparent changes in SEDs because the optically thick envelope reprocesses hot photons from the central region into cold emissions in the outer envelope as found also in Paper I.

A deep absorption feature at $10^{13.5}$ Hz (or 10 μm) corresponds to a striking feature in silicate. The absorption is extremely deep just before near-infrared emission appears in the SED. The deepness reflects the contrast in temperature between the cold region in the outer envelope, which is traced by the 10 μm feature, and hotter regions close to the center where near infrared photons are emitted. The absorption feature becomes shallower as the material in the envelope depletes because of the accretion onto the protostar.

The object would be detectable in near-infrared wavelengths at the last stages (curves 12 and 13). The SED labeled "12" shows typical features for class I protostars: a

large excess of the far-infrared component and undetectability in optical light. The SED labeled "13" corresponds to a more evolved YSO such as a class II object, for which the enhancement of luminosity in the far-infrared has disappeared and the peak in νF_ν has been shifted to the near-infrared. SED 13 shows a flat spectrum in the infrared and hence this object might correspond to a flat spectrum T Tauri star if the optical component appears in the SED owing to nonspherically-symmetric effects such as bipolar cavities (§ 4.2). We stopped the calculation at this stage because the further evolution of SED should involve a nonspherically symmetric treatment, where emissions from the circumstellar accretion disk and photons that escape through the bipolar cavities affect the SED in the near-infrared and the optical.

Figure 9 shows the SED in the initially hydrostatic model. One finds no essential difference from the initially homogeneous model (Fig. 8) except that the flux in the millimeter and submillimeter ($\nu < 12.5$ Hz) never decreases even at the final stage of the evolution. This is because our initially hydrostatic model contains a larger mass of the cloud core (§ 2.2) than the initially homogeneous model, which keeps providing the thermal emission of the infalling envelope in millimeter and submillimeter wavelengths. However, the spectral appearance in shorter wavelengths is quite insensitive to the initial density profile and, more remarkably, to the total mass (or the radius) of the initial cloud core. The reason for this is that the optical depth, $\tau = \int \kappa\rho\, dr$, is insensitive to the outer boundary when the density decreases with radius more rapidly than $\rho \propto r^{-1}$, which is the case in protostellar envelopes.

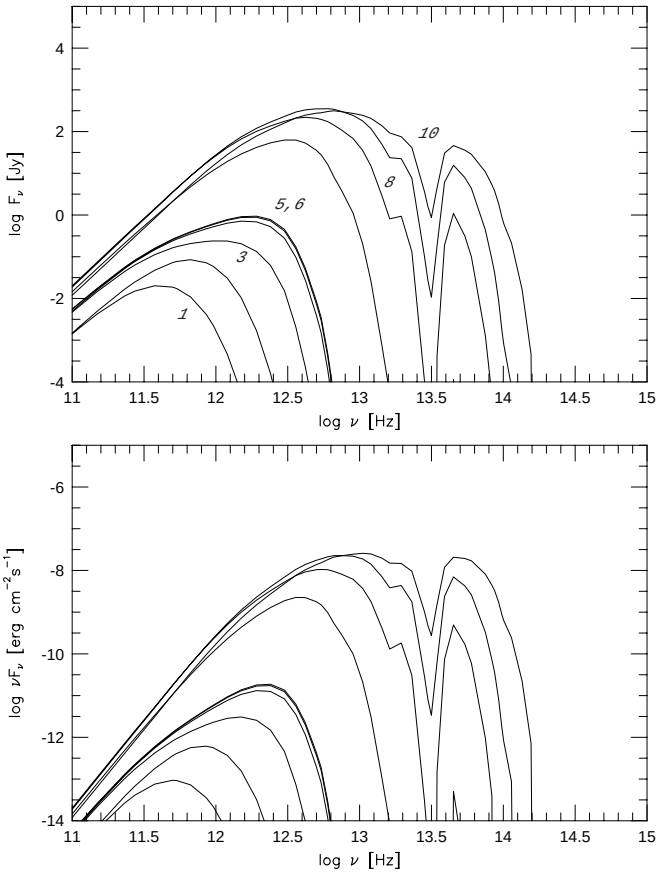

FIG. 9.—Evolution of the spectral energy distribution for the initially hydrostatic model is shown. Elapsed time of each curve is listed in Table 2. The upper panel delineates the emergent flux, F_ν, in units of Jy, while the lower depicts νF_ν in cgs units. An observer is assumed to be at a distance of 150 pc with a telescope of the resolution of 10″.

TABLE 2

ELAPSED TIMES FOR THE INITIALLY HYDROSTATIC MODEL

Label	$t - t_{0,e}$ (yr)[a]
1	-2.4674×10^5
2	-3.6097×10^4
3	-7.6469×10^2
4	-8.7500×10^{-1}
5	-1.7188×10^1
6	1.7656×10^0
8	2.1568×10^4
9	6.5776×10^4
10.....	1.7614×10^5

a The offset of time, $t_{0,e} \equiv 2.4674 \times 10^5$ yr, represents the instance when the second collapse begins.

4. DISCUSSION

In this section we discuss on possible interpretations of statistical trends in observations on the basis of our computational results. In § 4.1 we examine the bolometric temperature, which is a quantitative expression of SEDs, to relate our results with observed objects. Considering expected nonspherically symmetric effects, we illustrate an evolutionary picture of protostar formation in § 4.2.

4.1. *Bolometric Temperature*

As a quantitative measure of evolutionary status of YSOs, Myers & Ladd (1993) proposed the bolometric temperature, $T_{\rm bol}$, defined by

$$\frac{\int_0^\infty \nu B_\nu(T_{\rm bol})d\nu}{\int_0^\infty B_\nu(T_{\rm bol})d\nu} = \bar{\nu}\,, \tag{6}$$

where

$$\bar{\nu} \equiv \frac{\int_0^\infty \nu F_\nu\, d\nu}{\int_0^\infty F_\nu\, d\nu} \tag{7}$$

on the basis of an observed SED, F_ν. Combining equations (6) and (7), one obtains

$$T_{\rm bol} \equiv \frac{\zeta(4)}{4\zeta(5)}\frac{h\bar{\nu}}{k} = 1.25 \times 10^{-11}\bar{\nu}\ \text{Hz}^{-1}\text{K}\,, \tag{8}$$

where $\zeta(n)$ is the Riemann zeta function of argument n:

$$\zeta(n) \equiv \frac{1}{\Gamma(n)}\int_0^\infty \frac{t^{n-1}}{e^t - 1}dt\,. \tag{9}$$

Myers & Ladd (1993) showed that $T_{\rm bol}$ successfully distinguishes evolutionary positions of YSOs from protostars to weak-line T Tauri stars. Gregersen et al. (1997) found that the mean value of $T_{\rm bol}$ is 44 K for 16 class 0 sources.

To understand the statistical tendency in $T_{\rm bol}$ of observed protostars, we calculate the bolometric temperature from our SED (Fig. 10). The bolometric temperature monoton-

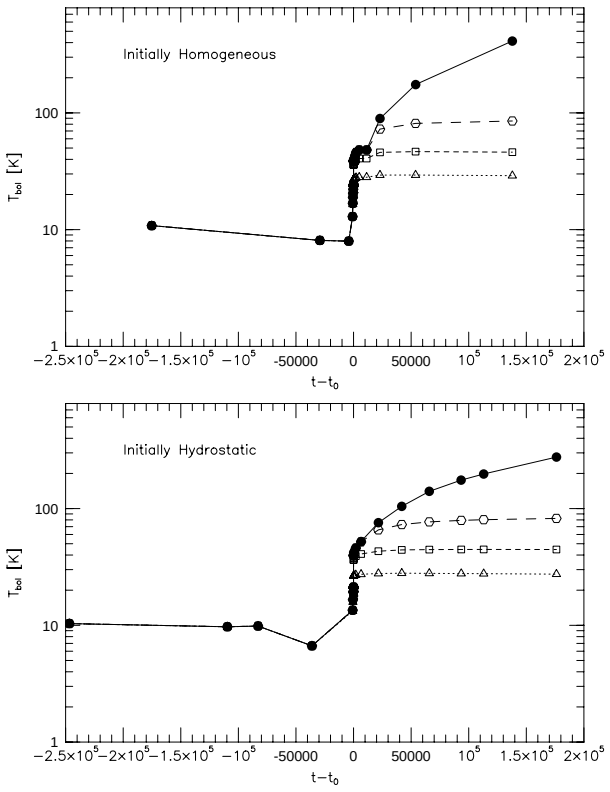

FIG. 10.—Evolution of the bolometric temperature, T_{bol}, is shown. The solid line delineates T_{bol} estimated by the original definition for $\bar{\nu}$ given by eq. (7). The other lines denote T_{bol} estimated using $\bar{\nu}$ with a upper cutoff frequency, f_c, in the integral (see text), where f_c is 3×10^{12} Hz for the dotted line, 5×10^{12} Hz for short-dashed line, and 1×10^{13} Hz for the long-dashed line. The upper panel is for the initially homogeneous model, and the lower panel isfor the initially hydrostatic model.

ically increases with time. While T_{bol} remains at 10 K before a protostar is formed ($t - t_0 < 0$), it abruptly rises up to 40 K after $t - t_0$ exceeds 0 and then gradually increases to 410 K. Chen et al. (1995) found that observed class 0 sources show T_{bol} less than 70 K, which corresponds to $t - t_0 \leq 2 \times 10^4$ yr in our results. This is smaller by an order of magnitude than the typical age of class I sources. We call these very young protostars as "genuine" class 0 objects. We find no essential differences in the evolution of T_{bol} between the initially homogeneous model and the initially hydrostatic model as expected from the discussion in § 3.3, in contrast to the luminosity curve (§ 3.2).

4.1.1. *Observational Implication to the Initial Condition*

The luminosity curve and T_{bol} in the computational results implies that genuine class 0 sources should be more luminous than class I sources for the initially homogeneous model, and less luminous for the initially hydrostatic model. Observations have revealed that the typical luminosities are $\sim 1\ L_\odot$ for class I sources (Kenyon et al. 1990) and $5.7\ L_\odot$ for class 0 sources (Gregersen et al. 1997). Obviously protostars in a younger phase tend to be more luminous, which supports the initially homogeneous model. Note that the "homogeneity" considered here is just for convenience, and any other initial density structures that are not in hydrostatic equilibrium would trace a dynamical evolution similar to the initially homogeneous model rather than to the initially hydrostatic model, as long as the initial cloud core is (marginally) Jeans unstable. A cloud core that is not in hydrostatic equilibrium obtains a relatively large $\dot{M}_*$ because of the initial inward acceleration, which leads to large luminosity just after the birth of a protostar (§ 3.2). In contrast, the initially hydrostatic model, where a lower $\dot{M}_*$ admits neither the rapid growth of a protostar nor the immediate exhaustion of the infalling material, fails to reproduce the qualitative tendency in the luminosity of observed YSOs and instead the luminosity increases gradually and monotonically. This implies that the observed evolution of luminosity does not favor the spontaneous mechanism of star formation (§ 2.2).

Nevertheless, we do not exclude the dissipation of turbulence (Nakano 1998) as a possible mechanism for initiating star formation in case that the "macroturbulence," where the scale length of turbulent fluctuations is comparable with the scale of the system and hence turbulent motions can no longer be treated as an effective sonic velocity, dominates the turbulent field because dissipation of macroturbulence would not necessarily produce a nearly hydrostatic cloud core when the dynamical collapse is initiated.

4.1.2. *Comments on the Generality of the Initial Condition*

An initially hydrostatic cloud core of 1 $M_\odot$, instead of 3.852 $M_\odot$ of our choice, would yield a declining luminosity curve due to the exhaustion of the infalling material as in the initially homogeneous case. This model, however, does not match the observations because it cannot produce sufficient luminosity at 2×10^4 yr, i.e., the genuine class 0 stage, to account for observed class 0 sources. The mean luminosity of observed class 0 sources is $5.7\ L_\odot$, but the genuine class 0 objects should be significantly more luminous because the contamination of heavily obscured (or class 0–like class I) sources should have lowered the mean luminosity of observed class 0. Furthermore, we can present as follows another evidence for our point that initially hydrostatic cloud cores do not reproduce the observational tendency. The decline of the luminosity curve is observed when the protostellar mass arrives at $\sim 0.5\ M_\odot$ in the initially homogeneous model of the total mass of 1 $M_\odot$ (Fig. 7). On the other hand, it takes 0.8×10^5 yr for a protostar to grow in mass to $0.5\ M_\odot$ in the initially hydrostatic model, while it is much earlier for the initially homogeneous model. This implies that the luminosity would turn to decrease at $t - t_0 = 0.8 \times 10^5$yr for an initially hydrostatic core of 1 $M_\odot$, or actually more later because a less massive hydrostatic core would provide a smaller mass accretion rate after a protostar is born as discussed in § 3.2. On the other hand, the class I stage has already begun before that time (see Fig. 11). Therefore the infalling material is exhausted too late to explain the observational trend of the decreasing luminosity from class 0 to class I for an initially hydrostatic cloud core even if the total mass is limited to 1 $M_\odot$.

It may be helpful to consider also a hydrostatic initial condition with a highly centrally concentrated profile, which corresponds to spontaneous star formation with the ambipolar diffusion of magnetic fields. In this case, the main accretion phase begins as the outer envelope remains in hydrostatic equilibrium since the free-fall time in the central region is quite short (§ 3.2) compared to the accretion time of the whole envelope. The obtained mass accretion rate, therefore, would be still much smaller and thus the luminosity curve would monotonically increase more gradually than in the marginally unstable hydrostatic case. This

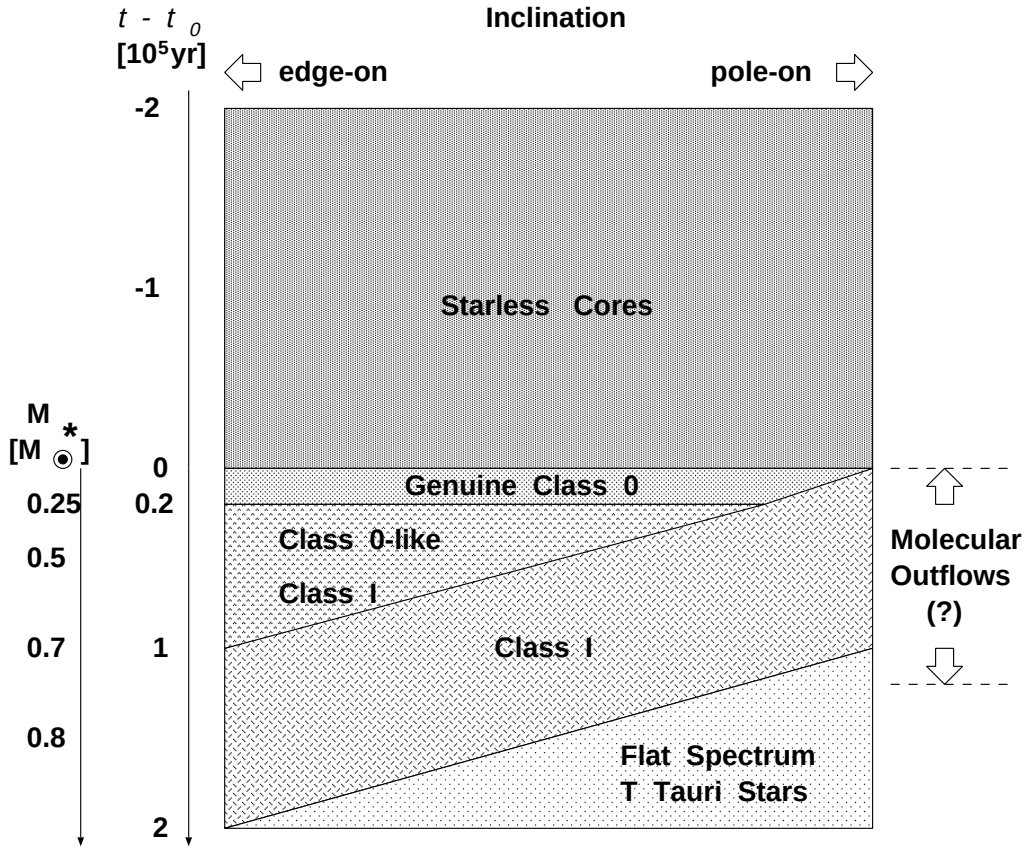

FIG. 11.—Schematic picture of the evolution of protostar formation is illustrated. The vertical axis represents the evolutionary time in the unit of 10^5 yr, where the offset value, t_0, indicates the instance of the birth of a protostar (see Table 1). The protostellar mass, M_*, is shown based on Fig. 7. The epoch in which outflows associate with YSOs is also indicated. The horizontal axis corresponds to the inclination angle of the YSO to an observer. The area occupied by each type of YSOs roughly corresponds to the number of the objects expected to be observed.

picture mimics the expansion-wave solution by Shu (1977), which has the minimum mass accretion rate, $0.975c_s^3/G$ at the origin, among the family of the inside-out solutions of the isothermal self-similar collapse.

4.1.3. *The Effect of the Circumstellar Disk*

Our calculations suppose spherical symmetry. Actually, each YSO can be observed as either class I or class 0 depending on its inclination angle to an observer because an edge-on view suffers from high column density, so that the object would be seen as if it were less evolved. To examine how much this effect modifies $T_{\rm bol}$, we also show in Figure 10 the bolometric temperatures which would be estimated if emissions were deficient in high frequencies. We calculate the mean frequency, $\bar{\nu}$, imposing an upper cutoff frequency, f_c, that is,

$$\bar{\nu} \equiv \frac{\int_0^{f_c} \nu F_\nu \, d\nu}{\int_0^{f_c} F_\nu \, d\nu} , \tag{10}$$

which is substituted for equation (7). Figure 10 indicates that $T_{\rm bol}$ is sensitive to f_c for 3×10^{12} Hz $< f_c < 1 \times 10^{13}$ Hz and $T_{\rm bol}$ can be significantly underestimated even after $t \sim 10^5$ when near infrared components are hidden by locally enhanced column density in the disk plane. A fraction of edge-on class I, or "class 0–like class I", would not be large relative to the total number of class I sources, but it can be substantially large compared to genuine class 0 sources, which are less abundant by an order of magnitude than class I sources. Hence the contamination of edge-on class I objects into class 0 sources is not negligible.

A clue for discriminating genuine class 0 objects from edge-on class I objects lies in the luminosity of individual sources since our initially homogeneous model shows that the luminosity reaches the maximum value of 25 $L_\odot$ at 2×10^4 yr, which corresponds to the typical age of genuine class 0, and the luminosity declines as the evolution proceeds. YSOs with cold $T_{\rm bol}$ that have luminosities considerably larger than 1 $L_\odot$ would be genuine class 0 objects. On the other hand, cold YSOs with comparable luminosities with class I sources are probably more evolved protostars than genuine class 0 objects. While the luminosity problem for class I objects can be resolved by a possible difference in the mass accretion rates between the circumstellar disk and the infalling envelope (§ 3.2), the luminosity problem would not arise for the protostars substantially younger than class I, where nonspherically symmetric effects are less important because a significant fraction of the angular momentum of the rotating cloud core still remains far away from the central protostar. Hence the large luminosity for genuine class 0 objects in our results, i.e., $\sim$25 $L_\odot$, would not seriously suffer from the luminosity problem.

Unfortunately, the bolometric luminosity estimated from observations suffers from a large uncertainty for such young protostars. A major fraction of the luminosity is emitted in the submillimeter and only an upper-limit value is obtained for the infrared flux. Furthermore, the luminosity of a YSO

on an edge-on view would be underestimated because only a small fraction of the total emission leaks out through the disk plane. Direct comparison of the observed luminosities with our numerical results require a great care.

4.2. *An Evolutionary Picture of Protostar Formation*

In the preceding section we established a theoretical model for protostar formation which accounts for recent observations. The theoretical treatment in this model is fully consistent in the framework of spherical symmetry, and thus the computational results including the age, luminosity, and bolometric temperature are quantitatively reliable. On the other hand, the physical structure of actual YSOs is not in spherical symmetry because of the effects due to rotation and magnetic fields. In this subsection we discuss possible contributions of these nonspherically-symmetric effects to our results.

We pointed out in § 3 that edge-on class I objects would be observed as class 0 sources ("class 0–like class I"), and they would contaminate the "genuine" class 0 objects which have the age of 2×10^4 yr and are substantially younger than class I sources. Similarly, evolved class I objects would be seen as flat spectrum T Tauri stars depending on the inclination angle to an observer.

Theoretical and observational evidence supports the idea that flat spectrum T Tauri stars are associated with circumstellar envelopes. Natta (1993) reproduced the observed flat spectra by considering the back-warming of the disk by scattered stellar photons in the envelope. Calvet et al. (1994) showed that the thermal emission from the extended envelope with a polar cavity forms the flat spectra in addition to the emission from the central star and disk. Kikuchi, Nakamoto, & Ogochi (2000) performed two-dimensional radiative transfer calculations and successfully produced the flat spectra by the back-warming of the disk by the scattering and thermal reprocessing of stellar photons in the envelope. Observations have revealed the presence of extended envelopes surrounding HL Tau (Hayashi, Ohashi, & Miyama 1993) and T Tauri (Momose et al. 1996), which are typical flat-spectrum T Tauri stars. T Tauri stars with flat spectra tend to have larger extinction than typical T Tauri stars (Osterloh & Beckwith 1995). A recent high-resolution observation (Close et al. 1997) succeeded in direct imaging of HL Tau in the near infrared. They confirmed the existence of bipolar cavities, through which optical photons from the central star escape out.

Compiling comprehensively our findings and other theoretical and observational evidence, we illustrate an evolutionary picture of protostar formation in Figure 11. Protostellar evolution proceeds from top to bottom. Before t reaches t_0, where $t_0 \sim 2 \times 10^5$ yr indicates the instance of the birth of a protostar (see Table 1 in § 3.1), a cloud core experiences gravitational collapse without any significant changes in SEDs (§ 3.3). Such cloud cores would be observed as starless cores even after the formation of the first core (Paper I). After a protostar is born ($t > t_0$), the appearance of a YSO depends not only upon the evolutionary time but on the inclination angle to an observer, which is indicated by the horizontal axis. A pole-on view enables an observer to see more deeply inside the protostellar envelope because the infalling material along the polar axis is swept up by the centrifugal force and the bipolar outflows. On the contrary, an edge-on view suffers from enhanced column density in the disk plane, which causes significant underestimation of the bolometric temperature (§ 3.3). A YSO at a certain evolutionary position is therefore observed as if it were more evolved on a pole-on view and less evolved on an edge-on view. This tendency is schematically illustrated in Figure 11. Observed class 0 sources consist of genuine class 0 objects and edge-on class I, or class 0–like class I, objects. A flat spectrum T Tauri star would be evolved to a typical classical T Tauri star as the circumstellar envelope is dispersed or exhausted.

The area occupied by each type of YSOs in Figure 11 roughly corresponds to the number of the objects expected to be observed. On the basis of this fact, one can give a constraint on the epoch in which molecular outflows associate with YSOs by considering a statistical trend in observations. Mardones et al. (1997) listed 23 class 0 sources and 24 class I, where 23 sources of class 0 (100%) and 18 sources of class I (75%) show evidence of outflows. Therefore, the outflow epoch should cover the whole region of genuine class 0 and class 0–like class I, and three-fourths of class I in Figure 11. If an outflow begins when the main accretion phase starts (i.e., $t = t_0$) as predicted by Tomisaka (1998), Figure 11 shows that outflows should continue until $t - t_0 \sim 1.3 \times 10^5$ yr to naturally reproduce the observations. This estimation is, of course, very crude because it assumes that outflows are driven universally and steadily in the same epoch regardless of the individuality of each object. More elaborate estimation requires a further progress in both observational and theoretical studies in the driving mechanism of outflows.

Class 0 sources are observed typically on edge-on views (Hirano et al. 1997). This fact is attributed to the contamination of edge-on class I (or class 0–like class I) in our picture. The inclination angle would be randomly distributed for genuine class 0 objects, but class 0–like class I objects should have large inclination angles.

A genuine class 0 object on a pole-on view may be seen as a class I source. Such an object would be very luminous (25 $L_\odot$, see § 3.2) and have a small protostellar mass (0.1 $M_\odot$). Momose et al. (1998) derived the protostellar mass as $\sim 0.1\ M_\odot$ for L1551 IRS5, whose luminosity is $\sim 30\ L_\odot$ (Cohen et al. 1984). Hence L1551 IRS5 may be a genuine class 0 object on a pole-on view, or with a polar cavity of a large opening angle, which enables infrared photons to escape out so that it appears as a class I object despite its extreme youth.

A more quantitative picture than Figure 11 should involve numerical calculations based on multidimensional radiation hydrodynamics. Such a calculation requires very large computational costs and is not yet available at present, but it will be a challenging task in future.

5. SUMMARY

Our findings in this paper are summarized as follow.

1. RHD numerical calculations are carried out to study physical processes in the formation of a 1 $M_\odot$ protostar. The whole evolution are pursued from the beginning of the first collapse to the end of the main accretion phase. All the physical phenomena that appear in protostellar formation, (e.g., the dynamical collapse of a cloud core, the formation of the pressure-supported core, the accretion shock front on the protostellar surface, and the supersonically infalling gas) are incorporated self-consistently in the calculations.

2. A protostar is born after the initial isothermal collapse of a cloud core (the first collapse) and the subsequent collapse triggered by dissociation of molecular hydrogen (the second collapse). The protostar grows in mass as accreting the infalling material from the circumstellar envelope while the protostar keeps its radius at $\sim 4\ R_\odot$ during the main accretion phase. These typical features in the evolution are in good agreement with previous studies.

3. For the initially homogeneous model, the accretion luminosity rapidly rises to the maximum value of $25\ L_\odot$ just after the formation of a protostar, and declines gradually as the mass accretion rate decreases. In contrast, the luminosity increases monotonically with time for the initially hydrostatic model. This discrepancy arises because the mass accretion rate varies depending inward acceleration at the initial stage, which affects the luminosity curve. Any hydrostatic cloud cores would yield only a gradual rise in the luminosity curve after the birth of a protostar unless the total mass is substantially larger than $3.852\ M_\odot$.

4. We confirm that the SED evolves from a 10 K graybody spectrum to hotter spectra typical for class I and flat spectrum sources. The bolometric temperature derived by the obtained SED shows that cold sources with $T_{\rm bol}$ less than 70 K are younger than 2×10^4 yr ("genuine" class 0 objects). This indicates that class 0 objects have younger ages by an order of magnitude than class I objects. However, $T_{\rm bol}$ can be significantly lower even after $t \sim 10^5$ yr if the infalling material with angular momentum falls onto a circumstellar disk and near-infrared components are hidden by locally enhanced column density in the disk plane. Observed class 0 sources should be the compound of the genuine class 0, which is as young as 10^4 yr, and more evolved protostars on edge-on view ("class 0–like class I"). The contamination of edge-on class I objects are not negligible because they are intrinsically abundant than genuine class 0 objects.

5. Since observations indicate that class 0 sources are typically more luminous than class I sources, the initially hydrostatic model, in which the luminosity increases monotonically with time, does not explain the observation. The initially homogeneous model, in contrast, shows the tendencies consistent with the observations. This implies that the observed evolution of luminosity does not favor the spontaneous mechanism of star formation. The decreasing luminosity with time implies that significantly luminous and cold YSOs ($L \gg 1\ L_\odot$ and $T_{\rm bol} < 70$ K) should be genuine class 0 objects. Less luminous YSOs are more evolved protostars on edge-on view even if they have cold $T_{\rm bol}$.

6. Finally, we propose an evolutionary picture of protostar formation compiling our findings in this paper and other theoretical and observational evidence. In terms of the evolutionary time and the inclination to an observer, protostellar objects are found to be clearly categorized.

In our numerical code, the convective energy transport and the nuclear energy production are not taken into account. The deuterium burning, which is ignited at $T \sim 10^6$K, should occur in the protostar at the final stage of our calculation.

These effects might change the structure of the protostar but a possible change would not be large because the available energy from the deuterium burning is not larger than the released energy by the quasi-static contraction of a protostar. Indeed, SST considered both the convection and deuterium burning and they found the protostellar radius of $3 \sim 4\ R_\odot$, which accords with our result quite well. Furthermore, a slight difference in the protostellar structure would give no influence on the structure of the infalling envelope. Hence the SEDs would remain unchanged by incorporating the convection and the nuclear reactions.

The authors are grateful to Shoken M. Miyama, Takenori Nakano, and Munetake Momose for their helpful comments and discussions. H. M. thanks Harold W. Yorke for his kindly sending me tabulated data of the dust opacities. Helpful comments and questions of the referee, Dean McLaughlin, with which some ambiguous points in the original version have become more clear and convincing. The research of H. M. is supported by the Research Fellowships of the Japan Society for the Promotion of Science for Young Scientists.

APPENDIX A

BASIC EQUATIONS

In spherical symmetrical Lagrangian (comoving) coordinates, the basic equations of radiation hydrodynamics are written as follows:

$$\frac{dr}{dt} = v\,, \tag{A1}$$

$$\rho = \frac{3}{4\pi}\frac{\partial M_r}{\partial (r^3)}\,, \tag{A2}$$

$$\frac{Dv}{Dt} = -\frac{GM_r}{r^2} - 4\pi r^2 \frac{\partial p}{\partial M_r} + \frac{\kappa_F^{\rm gas}}{c} F - \frac{v_Q}{\rho}\,, \tag{A3}$$

$$\frac{D}{Dt}\left(e + \frac{E}{\rho}\right) + (fE + p)\frac{D}{Dt}\left(\frac{1}{\rho}\right) - (3f - 1)\frac{v}{\rho r} E = \epsilon_{\rm CR} + \epsilon_Q - \Lambda_{\rm gd} - \frac{\partial (4\pi r^2 F)}{\partial M_r}\,, \tag{A4}$$

$$\frac{1}{c^2}\frac{DF}{Dt} + \frac{4\pi r^2 \rho}{q}\frac{\partial (fqE)}{\partial M_r} = -\frac{\chi_F F}{c}\,, \tag{A5}$$

$$\frac{De}{Dt} + p\frac{D}{Dt}\left(\frac{1}{\rho}\right) = (c\kappa_E^{\rm gas}E - 4\pi\kappa_P^{\rm gas}B) + \epsilon_{\rm CR} + \epsilon_Q - \Lambda_{\rm gd} \ . \tag{A6}$$

Here v_Q and ϵ_Q are taken from the tensor artificial viscosity in the formulation by Tscharnuter & Winkler (1979),

$$v_Q = \frac{9}{r}\frac{\partial}{\partial r^3}\left\{r^3 l^2 \rho \frac{\partial(r^2 v)}{\partial r^3}\left[\frac{\partial v}{\partial r} - \frac{\partial(r^2 v)}{\partial r^3}\right]\right\} ,$$

$$\epsilon_Q = -4.5 l^2 \frac{\partial(r^2 v)}{\partial r^3}\left[\frac{\partial v}{\partial r} - \frac{\partial(r^2 v)}{\partial r^3}\right]^2 ,$$

where l, a coefficient with dimension of length, is of the order of the local width of grid to smear out the shock front artificially so that the discretized hydrodynamic equations can handle shock waves. Both v_Q and ϵ_Q are switched to zero where $\nabla\cdot v > 0$, that is, the artificial viscosity works only when the gas is compressed.

The Eddington factor, f, and the frequency-averaged quantities are calculated based on solutions of the angle- and frequency-dependent radiative transfer equation according to the following equations:

$$f_\nu = \frac{K_\nu}{J_\nu} , \tag{A7}$$

$$\kappa_F = \frac{\int_0^\infty \kappa_\nu H_\nu \, d\nu}{H} , \tag{A8}$$

$$\kappa_E = \frac{\int_0^\infty \kappa_\nu J_\nu \, d\nu}{J} , \tag{A9}$$

$$\kappa_P = \frac{\int_0^\infty \kappa_\nu B_\nu \, d\nu}{\sigma T^4/\pi} , \tag{A10}$$

and

$$f = \frac{\int_0^\infty f_\nu J_\nu \, d\nu}{J} , \tag{A11}$$

where J_ν,H_ν, and K_ν are the first three moments of the monochromatic specific intensity, and those without a subscript ν are the values integrated over frequency. The sphericality factor q is defined by (Auer 1971)

$$\ln\ q = \int_{R_{\rm in}}^{r} \frac{3f - 1}{fr'} \, dr' \ .$$

Heating or cooling by collisions between gas and dust is taken into account through the energy exchange rate, $\Lambda_{\rm gd}$:

$$\Lambda_{\rm gd} = \sum_{(n)} \Lambda_{\rm gd}^{(n)} ,$$

where the superscript (n) denotes the dust components. We consider three components of dust grains, i.e., amorphous carbon, silicate, and dirty ice-coated silicate, on the basis of the dust model by Preibisch et al. (1993). The energy exchange rate for each dust component is expressed as (Hayashi & Nakano 1965; Leung 1975)

$$\Lambda_{\rm gd}^{(n)} = \frac{3}{2}\left(\frac{8k}{\pi m_{\rm H_2}}\right)^{1/2} \frac{n_{\rm H_2}}{\rho} n_{\rm gr}^{(n)}[\pi a^{(n)2}] T^{1/2} k[T - T_{\rm gr}^{(n)}] , \tag{A12}$$

where $n_{\rm gr}^{(n)}$ and $T_{\rm gr}^{(n)}$ are the number density and temperature of dust grains of component (n). The dust temperature is determined by (Hayashi & Nakano 1965),

$$\Lambda_{\rm gd}^{(n)} + \kappa_E^{(n),\rm abs} cE - 4\kappa_P^{(n),\rm abs}\sigma T_{\rm gr}^{(n)\,4} = 0 \ . \tag{A13}$$

The nuclear energy productions and the convective energy transport are not considered.

In earlier versions of the numerical code we imposed the condition that the transfer equation solver and the moment equations solver should be iterated until convergence is achieved to a desirable extent. One thus obtains the radiation hydrodynamic quantities which are consistent with the radiation field at each time step. While this procedure works well during calculations for the first collapse (Paper I), convergence is found to be much worse after the second collapse due to complicated behaviors of the Eddington factors near the accretion shock front. Therefore convergence between the transfer equation solver and the moment equations solver is not imposed in the present version of the code, where the transfer equation is solved once in several time steps under the constraint that the variations of the Eddington factors should not be too large.

In Eulerian coordinates, the basic equations (eqs. [A1]–[A6]) are rewritten into

$$\frac{\partial M_r}{\partial t} + 3vr^2 \frac{\partial M_r}{\partial r^3} = 0 , \tag{A14}$$

$$\rho = \frac{3}{4\pi}\frac{\partial M_r}{\partial r^3}, \tag{A15}$$

$$\frac{\partial v}{\partial t} + v\frac{\partial v}{\partial r} = -\frac{GM_r}{r^2} - \frac{\partial p}{\partial r} + \frac{\kappa_F^{\rm gas}}{c}F - \frac{v_Q}{\rho}, \tag{A16}$$

$$\frac{\partial}{\partial t}\left(e + \frac{E}{\rho}\right) + v\frac{\partial}{\partial r}\left(e + \frac{E}{\rho}\right) + (p + fE)\frac{3}{\rho}\frac{\partial(r^2 v)}{\partial r^3} - (3f - 1)E\frac{v}{\rho r} = \epsilon_{\rm CR} + \epsilon_Q - \Lambda_{\rm gd} - 3\frac{\partial(r^2 F)}{\partial r^3}, \tag{A17}$$

$$\frac{1}{c^2}\left(\frac{\partial F}{\partial t} + v\frac{\partial F}{\partial r}\right) + \frac{1}{q}\frac{\partial(fqE)}{\partial r} = -\frac{\chi_F F}{c}, \tag{A18}$$

and

$$\frac{\partial e}{\partial t} + v\frac{\partial e}{\partial r} + p\frac{3}{\rho}\frac{\partial(r^2 v)}{\partial r^3} = (c\kappa_E^{\rm gas}E - 4\pi\kappa_P^{\rm gas}B) + \epsilon_{\rm CR} + \epsilon_Q - \Lambda_{\rm gd}. \tag{A19}$$

Equations (A12) and (A13) remain unchanged.

In the initial collapse phase, highly concentrated density structure is developed in the center and hence Lagrangian coordinates are suited to the calculations. Lagrangian scheme, however, is not useful when a sharp structure such as a shock wave is generated in diffuse areas where grid points are sparsely distributed. By this reason, calculations are performed on Lagrangian coordinates for the initial isothermal collapse, and the Eulerian takes the place after the adiabatic core is formed—i.e., after the accretion shock is generated. This method was found to successfully resolve the accretion shock at the surface of the first and second cores in our calculations. In early versions of our code, second-order accurate advection (i.e., the van Leer advection) was adopted for Eulerian calculations, supplementing the Lagrangian RHD equations (A1)–(A6) (Paper I). This method works well for calculations at the first collapse stage but cannot be applied after the second collapse occurs. This is because the advection solver suffers from the CFL condition where the flow is supersonic and time steps become unacceptably small compared to the evolutionary timescale at late stages of protostellar collapse. Therefore the discretized equations in the Eulerian formulation (eqs. [A14]-[A19]) have to be directly incorporated into the linearized matrix, instead of employing the external advection terms solver. Since upstream differentiation of first-order accurate is adopted, this "direct Eulerian scheme" is inferior in accuracy to the "Lagrangian with the Eulerian remapping scheme" using the van Leer advection. Nevertheless, it has a great advantage that large CFL numbers are permitted and computational time is reduced to a reasonable extent.

REFERENCES

André, P., Ward-Thompson, D., & Barsony, M. 1993, ApJ, 406, 122
Alexander, D. R., & Ferguson, J. W. 1994, ApJ, 437, 879
Auer, L. H. 1971, J. Quant. Spectrosc. Radiat. Transfer, 11, 573
Balluch, M. 1988, A&A, 200, 58
Barsony, M. 1994, in Clouds, Cores, and Low Mass Stars, ed. D. P. Clements & R. Barvainis (Provo: ASP), 197
Bodenheimer, P., & Sweigart, A. 1968, ApJ, 152, 515
Bonner, W. B. 1956, MNRAS, 116, 351
Boss, A. P., & Yorke, H. W. 1995, ApJ, 439, L55
Calvet, N., Hartmann, L., Kenyon, S. J., & Whitney, B. A. 1994, ApJ, 434, 330
Chen, H., Myers, P. C., Ladd, E. F., Wood, D. O. S. 1995, ApJ, 445, 377
Close, L. M., Roddier, F., Northcott, M. J., Roddier, C., & Graves, J. E. 1997, ApJ, 478, 766
Cohen, M., Harvey, P. M., Schwartz, R. D., & Wilking, B. A. 1984, ApJ, 278, 671
Ebert, R. 1955, Z. Astrophys., 37, 217
Foster, P. N., & Chevalier, R. A. 1993, ApJ, 416, 303
Goldsmith, P. F., & Langer, W.D. 1978, ApJ, 222, 881
Gregersen, E. M., Evans, N. J., II, Zhou, S., & Choi, M. 1997, ApJ, 484, 256
Hayashi, C., & Nakano, T. 1965, Prog. Theor. Phys., 34, 754
Hayashi, M., Ohashi, N., & Miyama, S. M. 1993, ApJ, 418, L71
Hirano, N., Kameya, O, Mikami, H., Saito, S., Umemoto, T., & Yamamoto, S. 1997, ApJ, 478, 631
Hunter, C. 1977, ApJ, 218, 834
Iglesias, C. A., & Rogers, F. J. 1996, ApJ, 464, 943
Kenyon, S. J., Hartmann, L., Strom, K. M., & Strom, S. E. 1990, AJ, 99, 869
Kenyon, S. J., Calvet, N., & Hartmann, L. 1993, ApJ, 414, 676
Kikuchi, N., Nakamoto, T., & Ogochi, K. 2000, PASJ, submitted
Larson, R. B. 1969, MNRAS, 145, 271 (L69)
Leung, C. M. 1975, ApJ, 199, 340
Mardones, D., Myers, P. C., Tafalla, M., Wilner, D. J., Bachiller, R., & Garay, G. 1997, ApJ, 489, 719
Masunaga, H. 1999, Ph.D. thesis, Univ. Tokyo
Masunaga, H. & Inutsuka, S. 1999a, ApJ, 510, 822
———. 2000, ApJ, 535, in press
Masunaga, H., Miyama, S. M., & Inutsuka, S. 1998, ApJ, 495, 346 (Paper I)
Momose, M., Ohashi, N., Kawabe, R., Hayashi, M., & Nakano, T. 1996, ApJ, 470, 1001
Momose, M., Ohashi, N., Kawabe, R., Nakano, T., & Hayashi, M. 1998, ApJ, 504, 314
Myers, P. C., & Ladd, E. F. 1993, ApJ, 413, L47
Nakano, T. 1979, PASJ, 31, 697
———. 1998, ApJ, 494, 587
Nakano, T., Hasegawa, T., & Norman, C. 1995, ApJ, 450, 183
Natta, A. 1993, ApJ, 412, 761
Osterloh, M. & Beckwith, S. V. W. 1995, ApJ, 439, 288
Penston, M. V. 1969, MNRAS, 144, 425
Preibisch, Th., Ossenkopf, V., Yorke, H. W., & Henning, Th. 1993, A&A, 279, 577
Saumon, D., Chablier, G., & Van Horn, H. M. 1995, ApJS, 99, 713
Shu, F. H. 1977, ApJ, 214, 488
———. 1995, in Molecular Clouds and Star Formation, ed. C. Yuan & J. H. You (Singapore:World Scientific), 97
Stahler, S. W., Shu, F. H., & Taam, R. E. 1980, ApJ, 241, 637 (SST)
Tomisaka, K. 1998, ApJ, 502, L163
Tscharnuter, W. M., & Winkler, K.-H. 1979, Comput. Phys. Commun., 18, 171
Winkler, K.-H. A., & Newman, M. J. 1980a, ApJ, 236, 201 (WN)
———. 1980b, ApJ, 238, 311 (WN)
Yorke, H. W., Bodenheimer, P., & Laughlin, G. 1993, ApJ, 411, 274
———. 1995, ApJ, 443, 199